

## CRAB FLARES DUE TO TURBULENT DISSIPATION OF THE PULSAR STRIPED WIND

JONATHAN ZRAKE

Kavli Institute for Particle Astrophysics and Cosmology, Stanford University, SLAC National Accelerator Laboratory, Menlo Park, CA 94025, USA

*Draft version September 21, 2018*

### ABSTRACT

We interpret  $\gamma$ -ray flares from the Crab Nebula as the signature of turbulence in the pulsar’s electromagnetic outflow. Turbulence is triggered upstream by dynamical instability of the wind’s oscillating magnetic field, and accelerates non-thermal particles. On impacting the wind termination shock, those particles emit a distinct synchrotron component  $F_{\nu, \text{flare}}$ , which is constantly modulated by intermittency of the upstream plasma flow. Flares are observed when the high-energy cutoff of  $F_{\nu, \text{flare}}$  emerges above the fast-declining nebular emission around 0.1 - 1 GeV. Simulations carried out in the force-free electrodynamics approximation predict the striped wind to become fully turbulent well ahead of the wind termination shock, provided its terminal Lorentz factor is  $\lesssim 10^4$ .

*Subject headings:* pulsars: general — magnetohydrodynamics — magnetic reconnection — turbulence — gamma rays: stars — stars: winds, outflows

### 1. INTRODUCTION

Discovery of  $\gamma$ -ray flares from the Crab Nebula is among the foremost contributions to recent high-energy astrophysics. While it has now been five years since their announcement in 2011 (Tavani et al. 2011; Abdo et al. 2011), no longer wavelength counterparts have been established (Bietenholz et al. 2014; Kouzu et al. 2013; Bietenholz et al. 2014; Rudy et al. 2015; Madsen et al. 2015), and so the active region within the nebula remains unlocalized. The flares also present a formidable theoretical challenge because their power and duration cannot be accounted for within conventional theories of charged particle acceleration (e.g. Blandford et al. 2015a,b). Evidently, they are telling us something new — either about the nebula’s anatomy, or the physics of strongly magnetized plasma, or perhaps both.

Here we suggest Crab flares are the signature of an intermittent pulsar wind. Seen in this way, they provide empirical support for a turbulence resolution to the so-called  $\sigma$ -problem, referring to uncertainty over the mechanism by which the pulsar’s electromagnetic spin-down luminosity is diverted into particles (e.g. Kennel & Coroniti 1984; Emmering & Chevalier 1987). Pulsar wind plasma thus inherits spatial and temporal intermittencies that are characteristic of relativistic turbulence (Zrake & MacFadyen 2011, 2012; Radice & Rezzolla 2013), and flares can be produced when exceptionally large coherent structures transit the wind termination shock.

Our central assertion is that free energy associated with the pulsar’s alternating current (“striped wind”) destabilizes quickly, and is dissipated in the ensuing turbulent cascade. This view is supported by recent advances in the stability and reconnection processes of strongly magnetized plasma, (Uzdensky et al. 2010; Cerutti et al. 2014a; Sironi & Spitkovsky 2014; Guo et al. 2015; East et al. 2015; Zrake & East 2015), but differs with the conventional view that the striped wind is erased by steady magnetic reconnection through current layers that remain near equilibrium (Coroniti 1990; Lyubarsky & Kirk 2001; Kirk & Skjaraasen 2003).

Essential features of a model follow from this as-

sertion. First, we envision that synchrotron radiation is produced by supra-thermal electrons emerging from the wind zone into the compressed downstream magnetic field, so that photons may exceed the classical  $\sim 100$  MeV limit throughout the duration of electron cooling times. Second, we envision those electrons to be energized by turbulent dissipation in the flow well upstream of the wind termination shock. Finally, we attribute observed  $\gamma$ -ray variabilities to spatial intermittency of the upstream electron population; flares are seen when a gust of wind particles (henceforth a “blob”) sweeps across the wind termination shock along the line of sight. We will show that a model having these basic features can account for the flare duration and energetics without invoking explosive conversion of magnetic energy into radiation.

In Section 2.1 we summarize previous work on states of magnetized plasma resembling the striped wind. In Section 2.2 we estimate that current layers in the wind succumb quickly to linear instabilities. Then in Section 2.3 we simulate their subsequent non-linear evolution in the force-free electrodynamics approximation, finding that stripes are fully engulfed by turbulence after about two comoving dynamical times. In Section 2.4 we discuss freely decaying turbulence in a relativistically expanding background flow, and determine the maximum scale of coherent structures emerging from the wind region. In Section 3 we use those results to develop a simplistic model for the Crab Nebula flares. The model requires a wind Lorentz factor  $\Gamma \approx 2300$ , a post-shock magnetic field strength of 655 mG, and can be falsified by observation of flares about 5 times more powerful than the April 2011 event. In Section 4 we discuss limitations of the model and follow-up work that may validate certain assumptions.

### 2. TURBULENCE TRANSITION IN THE STRIPED WIND

#### 2.1. Free energy supply

Turbulence in the pulsar wind feeds on the oscillating magnetic field, or “stripes”. The stripes arise by rippling of the equatorial current sheet as the pulsar’s mag-

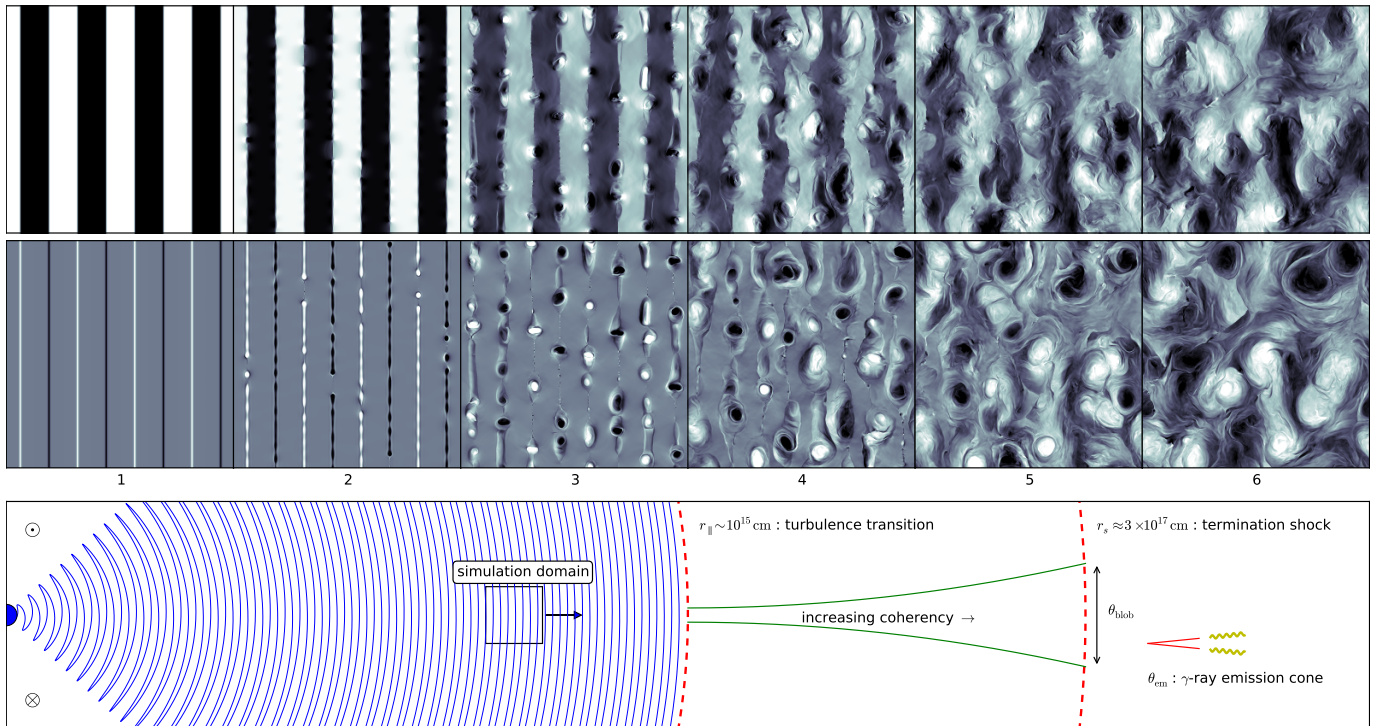


FIG. 1.— Transition to turbulence in the pulsar striped wind. Simulations were carried out for a local patch of wind in the plasma rest frame, using the force-free electrodynamics approximation. Shown are relief plot renderings made from two-dimensional subsets of three-dimensional data, with the toroidal (in-page) magnetic field component in the top panel, and the poloidal (out-of-page) component in the middle panel. The left-most column shows the initial condition given by Equation 3. The second column is shown just after saturation of a linear instability, and subsequent columns illustrate erasure of the stripes by transition to fully developed turbulence. Since the magnetic field weakens from left to right by turbulent dissipation, each image uses a color bar that is scaled to the instantaneous range of magnetic field values. The bottom panel (not to scale) shows a schematic diagram of the pulsar (blue circle), rippled current sheet (blue line), comoving simulation domain (square), and relative locations of the turbulence transition region  $r_{\parallel}$  and termination shock radius  $r_s$ .

netic dipole vector circles its spin axis, and are generic to plasma winds sourced by oblique rotators (Parker 1958; Coroniti 1990; Bogovalov 1999). As seen in the local rest frame of wind particles, they are an abundant source of magnetostatic free energy<sup>1</sup>. In earlier work, we found that such “excited” states of magnetized plasma were dynamically unstable (East et al. 2015), and promptly discharged their free energy through a turbulent cascade (Zrake & East 2015). The force-free equilibria ( $\mathbf{J} \times \mathbf{B} = 0$ ) we had considered were the short-wavelength Taylor states (Childress 1970; Dombre et al. 1986) which have uniform torsion  $\alpha \equiv \mathbf{J} \cdot \mathbf{B}/B^2$ . Although stripes are different in that  $\alpha$  is non-uniform (electrical current concentrates into thin layers around which the toroidal field switches sign), we will see in Section 2.3 that they similarly tend toward dynamical instability.

## 2.2. Linear instabilities

Turbulence can be induced by saturation of any small amplitude instability. Here, we estimate the growth rate of linear tearing modes affecting current layers (e.g. Biskamp 1986) between domains of opposite magnetic polarity. The upshot is that tearing modes saturate fast,

<sup>1</sup> A system’s magnetostatic free energy is what it can dissipate while respecting the frozen-in assumption ( $\mathbf{E} \cdot \mathbf{B} = 0$ ) in all but infinitesimal volumes. Such evolution conserves the system’s ideal topological invariants in the sense of Taylor (1974), while permitting conversion of magnetic energy into bulk motions and eventually heat.

so our conclusions would not change if another instability grows faster. Current layers in high Lundquist number plasma tend to form plasmoids (Bhattacharjee et al. 2009; Huang & Bhattacharjee 2010; Uzdensky et al. 2010), or become strongly corrugated (Inoue 2012). Our estimate here thus predicts how long current layers remain near equilibrium before such non-linear effects set in.

The fastest growing tearing mode has a wavelength comparable to the comoving layer thickness  $\tilde{a}$ , and a growth rate  $c\tilde{\lambda}_D^{-3/2}\tilde{a}^{1/2}$  when the plasma is hot (Zelenyi & Krasnosel’skikh 1979), where  $\tilde{\lambda}_D$  is the relativistic Debye length. Current layers collapse down to microscopic width  $\tilde{a} = \tilde{\lambda}_D$  (Michel 1994), so  $\tilde{\omega}_{\text{tear}} = c/\tilde{a}$ . As measured in the pulsar frame the current layer thickness near the light cylinder was found by Uzdensky & Spitkovsky (2014) to be  $a_L \approx 30$  cm. Plasma near the base of the wind is launched outward with a Lorentz factor  $\gamma_L \approx 200$  in the case of the Crab pulsar (Lyubarsky & Kirk 2001), so the comoving current layer thickness  $\tilde{a} = \gamma_L a$  is tens of meters. The tearing rate is a factor  $\gamma_L$  slower in the pulsar frame, and it slows further as the current layer inflates  $\propto r$  (charge density  $n_e \propto r^{-2}$  while  $\lambda_D \propto n_e^{-1/2}$ ),

$$\omega_{\text{tear}} = \gamma_L^{-2} \frac{c}{a_L} \left( \frac{r}{r_L} \right)^{-1}. \quad (1)$$

Near the light cylinder,  $\omega_{\text{tear}} \sim 10^4 \text{ s}^{-1}$ . By comparison, the Crab pulsar angular frequency  $\Omega \approx 190$ . In principle

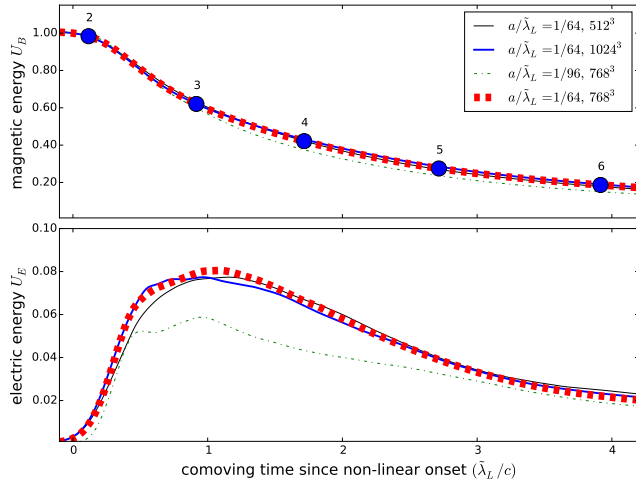


FIG. 2.— Time series of the integrated magnetic (top) and electric (bottom) energy in the simulation depicted in Figure 1. Time is measured since the onset of non-linear evolution, in units of the comoving light-travel time between stripes  $\tilde{\lambda}_L/c$ . Different curves show the same model at different grid resolution. The numbered blue circles correspond to the columns of Figure 1.

the tearing mode could be suppressed by inflation of the layer. However, the ratio of  $\omega_{\text{tear}}$  to the layer expansion rate  $\omega_{\text{exp}} = c/r$  is given by  $\gamma_L^{-2} r_L/a_L \sim 100$  independent of distance, so expansion may be safely neglected. The same also implies that tearing modes complete  $\sim 100$  exponential foldings in the vicinity of the wind’s base. We conclude that linear instability only characterizes the striped wind at extremely small radii  $r \ll r_s$ , and that evolution throughout the vast majority of its flight to the termination shock takes place in the non-linear regime.

### 2.3. Simulations

In order to illustrate non-linear evolution of the striped wind, we have carried out time-dependent numerical simulations in the plasma rest frame. We assume that the wind’s  $\sigma$  parameter is sufficiently high that the force-free electrodynamics (FFE) approximation is appropriate. FFE corresponds to the limiting case of relativistic magnetohydrodynamics (MHD) where electromagnetic contributions to the stress-energy tensor dominate those of matter. Use of continuum rather than fully kinetic formalism is justified by the same argument given in Section 2.2, namely that each wavelength contains millions to billions of plasma skin depths. FFE is formulated as Maxwell’s equations, together with the Ohm’s law

$$\mathbf{J} = \frac{\mathbf{B}}{B^2} (\mathbf{B} \cdot \nabla \times \mathbf{B} - \mathbf{E} \cdot \nabla \times \mathbf{E}) + \frac{\mathbf{E} \times \mathbf{B}}{B^2} \rho, \quad (2)$$

that follows from imposing perfect conductivity  $\mathbf{E} \cdot \mathbf{B} = 0$  and the force-free condition  $\rho \mathbf{E} + \mathbf{J} \times \mathbf{B} = 0$  (e.g. McKinney 2006). We use a numerical scheme that is fourth order accurate in space and time. Details are given in Zrake & East (2015).

Current layers in a striped wind collapse to an equilibrium supported by gas pressure as in the solution of Harris (1962). Since FFE neglects gas pressure, we instead construct our initial data as a sequence of force-free rotational current layers, that are in equilibrium by virtue of

uniform magnetic pressure ( $B^2 = \text{const}$ ) and vanishing tension density ( $\mathbf{B} \cdot \nabla \mathbf{B} = 0$ ). All such force-free equilibrium fields may be parameterized by the angle  $\phi(x)$  of the magnetic field vector in the transverse plane, as a function of longitudinal position  $x$  (where  $x$  is measured as a fraction of the domain length  $N_{\text{layer}} \tilde{\lambda}_L/2$ );  $\mathbf{B} = B_0 (\cos \phi(x), \sin \phi(x), 0)$ . In order to model current layers having width  $a$ , we choose  $\phi(x)$  to increase over the domain in a series of  $N_{\text{layer}}$  steps,

$$\phi(x) = \pi \sum_{n=1}^{2N_{\text{layer}}} \Theta_a \left( x - \frac{2n-1}{2N_{\text{layer}}} \right), \quad (3)$$

where  $\Theta_a(x) = \frac{1}{2} (1 + \tanh x/a)$  is a “smoothed” Heaviside step function. Even though our current layers are force-free rather than supported by gas pressure, they still admit a small-amplitude instability not unlike the tearing mode. A full description of that instability is outside the present scope; for our purposes it suffices to say that its growth rate was seen to increase as  $a$  decreases and that saturation is reached after a few dynamical times  $a/c$ . Once non-linear effects set in, the limited range of length scales becomes tolerable due to universality of the turbulent cascade with respect to small-scale closure, which we will give evidence for momentarily.

Our simulations are run on the triple periodic domain of size  $N_{\text{layer}} \tilde{\lambda}_L/2$ , where  $N_{\text{layer}} = 8$  and the grid resolution was  $512^3$ ,  $768^3$ , or  $1024^3$ . The current layer width  $a$  was varied between  $1/64$  and  $1/96$  of the stripe wavelength  $\tilde{\lambda}_L$ . We neglect transverse stretching, as well as longitudinal acceleration that may arise from heating of the plasma (e.g. Kirk & Skjaraasen 2003). Simulations are initiated in the force-free equilibrium state given by Equation 3, where the electric field is zero apart from a low amplitude ( $10^{-6}$ ) white-noise perturbation introduced to break translational symmetry along the layers.

Figure 1 contains renderings of two-dimensional slices of the toroidal (in-page, top panel) and poloidal (out-of-page, middle panel) magnetic field component. The left-most column shows the initial condition as described in Equation 3. The second column depicts the system when the linear instability first gives way to large-amplitude effects. By the third column, an ensemble of plasmoids (flux tubes oriented out of the page) has emerged. An important feature of these structures is that they would be long-lived were translational symmetry along their axis to be imposed, as was shown in Zrake & East (2015). Without imposing that symmetry, the flux tubes are unstable to kink and sausage modes. They also tend to coalesce with other flux tubes whose current flows in the same direction. This latter effect exemplifies the mechanism of non-helical inverse energy transfer studied in Zrake (2014). Subsequent columns portray the transition to fully developed turbulence. The whole sequence takes place over roughly 4 comoving light-travel times  $\tilde{\lambda}_L/c$  of a stripe, which is also the elapsed time experienced by plasma elements in transit from pulsar to termination shock when their Lorentz factor is  $\sim 10^4$ . In Figure 2 we plot the time series of volume-averaged magnetic and electric energy for different grid resolutions. Relative consistency among different parameters indicates that the rate of energy dissipation by turbulence is insen-

sitive to the current layer width and grid resolution, supporting the view that evolution in the non-linear regime is universal with respect to unresolved physics.

#### 2.4. Causality

Transition to turbulence occurs when plasmoids grow to the scale of the stripe separation  $\tilde{\lambda}_L$ . Our results from Section 2.3 indicate this occurs (fourth column of Figure 1) after a comoving fast magnetosonic time  $\tilde{\lambda}_L/\tilde{v}_f$ , that is when causal contact between stripes is first established. For a wind that moves with constant velocity  $v_w$ , this occurs at the radius <sup>2</sup>

$$r_{\parallel} = \frac{1}{2}\lambda_L \frac{v_w}{\tilde{v}_f} \left( \frac{1 - v_w^2 \tilde{v}_f^2 / c^4}{1 - v_w^2 / c^2} \right). \quad (4)$$

As shown in Figure 2, about half the magnetic energy has been dissipated by the time plasmoids reach the stripe scale, so prior evolution occurs in the regime where  $\tilde{v}_f$  is only somewhat smaller than  $c$  and the flow is super-fast magnetosonic,  $\tilde{\gamma}_f \ll \Gamma$  (Lorentz factors corresponding to  $\tilde{v}_f$  and  $v_w$ ). In that limit, Equation 4 gives us  $r_{\parallel} \approx \Gamma^2 \lambda_L$ . During this phase, the flow is likely to accelerate outward due to loss of inward tension provided by the toroidal magnetic field, and also by establishing a turbulent pressure gradient. A detailed analysis along the lines of Lyubarsky & Kirk (2001), together with a turbulence closure of the MHD equations would thus be necessary to determine the acceleration profile. Here, we adopt the conservative approximation that  $v_w$  appearing in Equation 4 corresponds to the terminal wind Lorentz factor. Transition to turbulence would thus be avoided by causality if  $\Gamma$  were to be  $\gtrsim 10^4$ . Faster winds would reach the deceleration point before a signal travels between adjacent current layers, so corrugations could not grow large enough to effect mixing between them. In Section 3 we will constrain  $\Gamma$  empirically within our interpretation of the Crab flares.

The third column of Figure 1 shows our prediction for the stripe morphology when the wind passes through  $r_{\parallel}$ , that is after a comoving fast magnetosonic time has elapsed since the onset of non-linear evolution. Beyond a few times  $r_{\parallel}$ , the wind evolves as freely decaying turbulence of magnetized relativistic plasma. The fully developed turbulent cascade could in principle be slowed by transverse expansion of the flow, so we need to repeat the exercise of Section 2.2, now comparing the eddy turn-over frequency  $\omega_e = v_A/\lambda_e$  with the expansion rate  $\omega_{\text{exp}} = c/r$ . Here, we have invoked that turbulent motions decay alongside the Alfvén speed  $v_A$  (Zrake 2014). As seen in the plasma rest frame (Figure 1), eddies are initially isotropic and roughly the size of the comoving stripe separation  $\tilde{\lambda}_L$ . They are thus seen in the pulsar frame to be stretched by a factor  $\Gamma$  in the transverse direction. Since we wish to compare transverse stretching rate with the eddy frequency, we assign eddies the transverse scale,  $\lambda_e = \Gamma \lambda_L$ . Keeping in mind that turbulent cells increase in size  $\propto r$  due to the expansion, as well as by inverse energy transfer (Zrake 2014; Brandenburg

et al. 2015; Olesen 2015), the eddy size is parameterized by  $\lambda_e = \Gamma \lambda_L (r/r_{\parallel})^{1+\delta}$  where  $\delta \geq 0$  determines the rate at which turbulence increases its coherence scale due to inverse energy transfer alone. The ratio of eddy turnover to expansion is thus

$$\frac{\omega_e}{\omega_{\text{exp}}} = \Gamma \left( \frac{\sigma}{1 + \sigma} \right)^{1/2} \left( \frac{r}{r_{\parallel}} \right)^{-\delta}, \quad (5)$$

where we have related  $\sigma$  to the Alfvén speed and assumed that  $\tilde{v}_f$  and  $v_w$  are both effectively  $c$  out to  $r_{\parallel}$ . Thus, at least out to a few  $r_{\parallel}$ , expansion can be safely neglected, and our simulation results (which do not account for that expansion) remain applicable.

What if turbulence evolves to increase its coherency at the fastest rate allowed by causality? Suppose that two fluid elements on radial trajectories with Lorentz factor  $\Gamma$  are initially at radius  $r_0$  and separated by an angle  $\theta$ . A pulse of light emitted by one is first received by the other when they have moved to a radius  $r_1 \approx r_0 \Gamma^2 \theta^2$ , provided<sup>3</sup>  $\Gamma \gg \theta^{-1}$ . By assuming that turbulence commences at  $r_0 = r_{\parallel}$  and setting  $r_1 = r_s$ , we determine the maximum angular coherence scale at the termination shock to be

$$\theta_{e,\text{max}} \sim \left( \frac{r_s}{\lambda_L} \right)^{1/2} \Gamma^{-2}. \quad (6)$$

### 3. A MODEL FOR THE CRAB NEBULA $\gamma$ -RAY FLARES

Here we develop a simplistic model for the Crab Nebula’s observed  $\gamma$ -ray variability (Tavani et al. 2011; Abdo et al. 2011; Balbo et al. 2011; Buehler et al. 2012; Striani et al. 2013; Rudy et al. 2015). We adopt a tentative interpretation of the April 2011 event in which the rise time  $\tau_{\text{rise}} \approx 10$  hr coincides with the emergence of a giant coherent structure (or “blob”) from the upstream wind into the post-shock flow, while the decline  $\tau_{\text{dec}} \approx 2$  days is associated with the cooling time of the blob’s highest energy particles.

We assume the shock’s kinetic structure to be mediated by energy-bearing particles having Lorentz factor  $\Gamma$ , while those of highest energy  $\gamma_{\text{max}} \gg \Gamma$  are only weakly deflected through an angle  $\theta_{\text{def}}$  before cooling in the post-shock magnetic field  $B_s$ . The angular scale  $\theta_{\text{em}}$  from which photons are received is the larger of  $\gamma_{\text{max}}^{-1}$  and  $\theta_{\text{def}}$ , and is reliably the latter. We assume that only a small patch of the blob surface is visible,  $\theta_{\text{blob}} > \theta_{\text{em}}$ , so that the flare’s inferred isotropic luminosity is independent of  $\theta_{\text{em}}$ . A further assumption is that turbulence develops similar longitudinal and transverse coherency in the pulsar rest frame. Though harder to justify (eddies typically emerge from the wind pancaked by Lorentz contraction), this condition only needs to be fulfilled intermittently both in time and solid angle. By setting  $\theta_{\text{blob}} = \theta_{e,\text{max}}$  (Equation 6), and  $r_s \theta_{\text{blob}} = c \tau_{\text{rise}} \approx 10^{15}$  cm where  $r_s \approx 3 \times 10^{17}$  cm, the bulk Lorentz factor is determined to be

$$\Gamma \approx \left( \frac{r_s}{c \tau_{\text{rise}}} \right)^{1/2} \left( \frac{r_s}{\lambda_L} \right)^{1/4} \approx 2.3 \times 10^3. \quad (7)$$

Next, we assume that particles emerge from the wind

<sup>2</sup> The expression for  $r_{\parallel}$  in Equation 4 reflects the distance at which two fast magnetosonic waves first meet, one propagating downstream starting at  $r = 0$ , and another in the upstream direction from  $r = \lambda_L$ .

<sup>3</sup> The exact answer is  $r_1/r_0 = f + \sqrt{f^2 - 1}$  where  $f = \Gamma^2 (1 - \cos \theta) + \cos \theta$ .

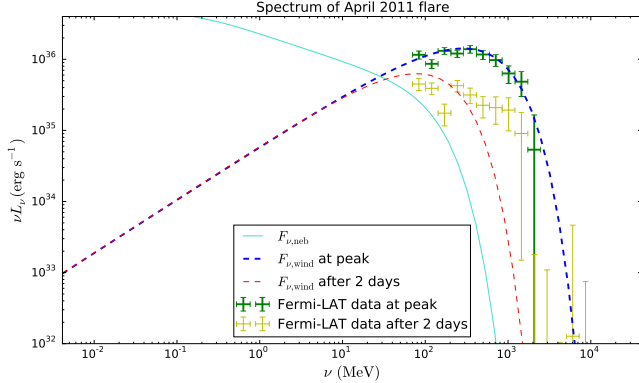


FIG. 3.— The quiescent Crab Nebula synchrotron spectrum, shown together with the flaring component shortly after the peak of the April 2011 event, and then another 2 days later.

with a power-law distribution  $f_{\text{flare}}(\gamma) \propto \gamma^{-p}$  between  $\Gamma$  and  $\gamma_{\text{max}}$ . We adopt the spectral index  $p = 3/2$  found in kinetic simulations of relativistic magnetic reconnection (Sironi & Spitkovsky 2014). The total number of emitting particles is given by

$$\varepsilon_e \dot{N} \tau_{\text{rise}} = \int_{\Gamma}^{\gamma_{\text{max}}} f_{\text{flare}}(\gamma) d\gamma \quad (8)$$

where  $\varepsilon_e$  is the fraction of  $\dot{N}$  that became non-thermal within the blob. Equating the flare duration  $\tau_{\text{dec}} \approx 2$  days with the cooling time of electrons moving with  $\gamma_{\text{max}}$  in the post-shock magnetic field, we find  $B_s \approx 1.7 \text{ mG } \gamma_{\text{max},9}^{-1/2}$ . The remaining free parameters are  $\gamma_{\text{max}}$  and the rate  $\varepsilon_e \dot{N}$  of non-thermal particles emerging from the wind with an angle  $\theta_{\text{em}}$  around the line of sight. They are determined by fitting Fermi-LAT data at the peak of the April 2011 flare to the synchrotron photon spectrum  $F_{\nu, \text{flare}}$  of the flaring component,

$$F_{\nu, \text{flare}} = \int_{\Gamma}^{\gamma_{\text{max}}} P_\nu f_{\text{flare}}(\gamma) d\gamma \quad (9)$$

where  $P_\nu$  is the specific synchrotron power per unit energy (Rybicki & Lightman 1979). We then evolve  $f_{\text{flare}}(\gamma)$  by synchrotron cooling in the post-shock magnetic field to determine the spectrum at later times.

Figure 3 shows  $F_{\nu, \text{flare}}$  fitted to the peak of the April 2011 flare, using Fermi-LAT data around MJD 55667 (Buehler et al. 2012), while Figure 4 shows the Fermi-LAT photon flux light curve above 100 MeV together with post-shock cooling of  $f_{\text{flare}}$ . The best-fit magnetic field value  $B_s = 655 \mu\text{G}$  is somewhat higher than the mean nebular field of  $124 \mu\text{G}$  (Meyer et al. 2010), but that is not unexpected in such close proximity to the shock. The corresponding maximum Lorentz factor is  $\gamma_{\text{max}} = 7 \times 10^9$ . The best-fit injection rate of non-thermal particles is  $\varepsilon_e \dot{N} = 2.2 \times 10^{37} \text{ s}^{-1}$ , which corresponds to an average non-thermal power supply of  $5.3 \times 10^{37} \text{ erg/s}$  throughout  $\tau_{\text{rise}}$  and within an angle  $\theta_{\text{blob}}$  of the line of sight. The former is 22% of the pulsar’s conventionally adopted production rate  $\dot{N} \sim 10^{38} \text{ s}^{-1}$  (Rees & Gunn 1974; Coroniti 1990)<sup>4</sup>, while the latter is 11% of the

<sup>4</sup> Particle production rates  $\gtrsim 10^{40} \text{ s}^{-1}$  for the Crab pulsar are inferred assuming the nebula electron population derives directly

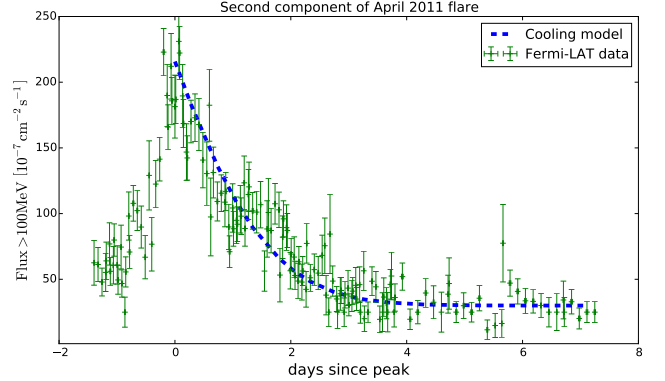


FIG. 4.— Decline of the second component of the April 2011 flare. Shown is the Fermi-LAT photon flux above 100 MeV between MJD 55666 and 55674, together with the model with  $B_s = 655 \mu\text{G}$  and  $\gamma_{\text{max}} = 7 \times 10^9$ .

isotropic pulsar spin-down power  $L = 4.6 \times 10^{38} \text{ erg/s}$  (Komissarov 2012). A bulk Lorentz factor  $\Gamma \approx 2300$  is much smaller than the Kennel & Coroniti (1984) value of  $\sim 10^6$ , but comparable to that of Tanaka & Takahara (2010) who estimate  $\Gamma \approx 7 \times 10^3$ . Kinetic studies of relativistic reconnection in strongly magnetized plasma agree on values of  $\varepsilon_e \sim 1$  (Guo et al. 2015; Sironi & Spitkovsky 2014).

If the post-shock magnetic field were to be coherent over  $c\tau_{\text{cool}} \approx 5 \times 10^{15} \text{ cm}$ , then particles moving with  $\gamma_{\text{max}}$  would be deflected through an angle  $\omega_g \tau_{\text{cool}} \approx 10^2 \theta_{\text{blob}}$ . Thus downstream trajectories must be in the Bohm limit to satisfy our assumption that  $\theta_{\text{em}} < \theta_{\text{blob}}$ . However, magnetic field correlations would need to vanish at scales  $\lambda_B \gtrsim 10^6 \text{ cm}$  for radiation to be in the jitter regime,  $\gamma_{\text{max}}^{-1} < \omega_g \lambda_B / c$  (Kelner et al. 2013).

#### 4. DISCUSSION

We have argued that the Crab Nebula’s  $\gamma$ -ray variability can be induced by turbulent intermittency of the pulsar wind. Our analysis predicts that linear instability of the current layers gives way to turbulence well upstream of the wind termination shock, provided the bulk Lorentz factor is  $\lesssim 10^4$ . We went on to estimate the largest spatial coherency attainable by freely decaying turbulence in the radially expanding flow, and found that the  $\sim 10$  hr rise time of the April 2011 event can be accounted for if  $\Gamma \approx 2300$ . We then fit a simplistic model to the Fermi-LAT spectrum of the flare, and determined roughly 1/10 of the pulsar’s spin-down luminosity must be channeled into non-thermal particles to explain it.

##### 4.1. Limitations

Our numerical treatment here was limited to a local co-moving patch of wind plasma. A more realistic analysis will need to account for expansion in the radial background flow, which could modify the nature of linear instabilities. We have also ignored all kinetic processes, which may complicate arguments given in Section 2.2 that linear instabilities act quickly. Still, we note that kinetic particle-in-cell simulations (Sironi & Spitkovsky 2011; Hoshino 2012) also point to large-scale disruption

from the pulsar (Bucciantini et al. 2011).

of striped magnetic fields not unlike the behavior in force-free electrodynamics simulations seen here.

We have also approximated the pulsar wind as having constant Lorentz factor as a function of radius, even though one dimensional MHD solutions involve acceleration due to both ideal (e.g. Michel 1973) and dissipative (e.g. Lyubarsky & Kirk 2001) processes. Such acceleration would follow the turbulence transition (due to loss of the inward tension force provided by the toroidal field), leading to suppression of causal contact and thus limiting the growth of coherent structures, which are crucial to our interpretation of the Crab Nebula flares. However, we have also ignored the prospect that current layers disrupt at close distance to the pulsar, when the Lorentz factor is still  $\lesssim 10^2$ . That would allow turbulence more time over which to develop spatial coherency. Our analysis of the tearing instability in Section 2.2 implies that appearance of plasmoids in the vicinity of the light cylinder is certainly possible. Actually, such behavior is an essential feature of the pulsed GeV emission scenario for the Crab pulsar sketched in Uzdensky & Spitkovsky (2014). Large-amplitude kinking of the current layer near the light cylinder in axially symmetric aligned rotator solutions has also been reported by Cerutti et al. (2015). Such early disruption would imply rapid acceleration very close to the wind’s base. Interestingly, abrupt acceleration of the wind at around  $30r_L$  has been inferred from the Crab’s pulsed emission in the very high energy  $\gamma$ -rays by Aharonian et al. (2012).

#### 4.2. Radiative efficiency of the wind zone

Very little radiation will be produced in the wind zone, even if it becomes turbulent. The reason is seen to be that comoving synchrotron power  $\propto \tilde{B}^2 \tilde{\gamma}$  is suppressed by a factor of  $\Gamma^2$ , while the travel duration is shortened by another factor of  $\Gamma$ . Specifically, a single particle traveling from radius  $r_0$  to the termination shock with Lorentz factor  $\gamma$  will radiate a fraction  $\varepsilon_{\text{rad}}$  of its kinetic energy given by

$$\int_{r_0}^{r_s} \omega_{\text{sync}} dt = \frac{2 r_e^2 r_L B_L^2}{3 m_e c^2} \Gamma^{-3} \gamma \left( \frac{r_L}{r_0} - \frac{r_L}{r_s} \right) \quad (10)$$

where  $\omega_{\text{sync}} = P_{\text{sync}}/\gamma m_e c^2$ ,  $r_e$  is the classical electron radius, and the magnetic field  $B_L(r/r_L)^{-1}$  is the upper limit corresponding to no dissipation. Assuming that  $B_L \approx 10^6$  G and that radiation begins around the turbulence transition  $r_0 = r_{\parallel}$ , we find that

$$\varepsilon_{\text{rad}} < 2.1 \times 10^{-6} \left( \frac{\gamma_{\text{max}}}{7 \times 10^9} \right) \left( \frac{\Gamma}{2300} \right)^{-5}. \quad (11)$$

#### 4.3. Comparison with other models

Our model for Crab flares has several features in common with the ideas of other authors. For example, the “magnetic untwisting” scenario of Sturrock & Aschwanden (2012) also envisions energy release to originate around  $10^{13} - 10^{15}$  cm, well within the wind zone. While our analysis indicates that significant dissipation of magnetic energy is possible there, poor radiative efficiency implies that any flaring emission could not be produced *in situ*. Teraki & Takahara (2013) have also developed a model in which flares occur when blobs emerge

from the wind zone, and examined the possibility that radiation occurs in the jitter regime. Our analysis provides a physical basis for the production of such blobs, but we find the condition for jitter radiation, namely that post-shock magnetic coherency peaks at  $\sim 10^6$  cm (Section 3), to be quite strict, as the relaxation time for such small-scale turbulence is extremely short. Bykov et al. (2012) proposed the flares correspond to rarest excursions in magnetic field intensity of plasma moving through the termination shock, which elicit radiative enhancements from an otherwise stationary electron population. That scenario also looks favorable if the pulsar wind contains turbulence. More conclusive evidence regarding possible TeV counterparts may help determine whether radiative intermittency originates in the particle distribution or magnetic field (Bednarek & Idec 2011). Future analysis aiming to measure the spatial statistics of magnetic versus non-thermal energy density in decaying plasma turbulence could also be fruitful.

Another avenue that looks encouraging if the inner wind contains turbulence is one in which flares occur when the termination shock normal moves through the line of sight due to its own intrinsic fluctuations (Camus et al. 2009). Such a scenario may treat values of  $\varepsilon_e \dot{N}$  and  $\gamma_{\text{max}}$  we inferred in Section 3 as reflecting *continuous* wind parameters, and that intermittency is introduced by fluctuations in the angle of the post-shock flow. We opted to explore the “blob” model for this work because of the appearance that Crab flare light curves are not time-symmetric, it because it allowed us to exploit the connection between the wind Lorentz factor and turbulence coherence scale discussed in Section 2.4. If further data indicates equal rise and decline times, or if the rather low Lorentz factor implied by our model can be independently ruled out, then the fluctuating termination shock approach seems to be a good choice. At least, it benefits from high efficiency of particle acceleration expected if turbulence operates throughout the far upstream flow.

Flares have also been suggested to occur by spontaneous magnetic reconnection events occurring somewhere in the nebula (Uzdensky et al. 2011; Clausen-Brown & Lyutikov 2012; Cerutti et al. 2014a,b). While relativistic magnetic reconnection is now understood to energize non-thermal particles with high efficiency, the April 2011 event requires *all* the magnetic energy (if released isotropically) in a region  $\sim 10^{16}$  cm with  $\sim$  mG intensity to be promptly converted into *fast-cooling* electrons. Thus, special reconnection geometries (“mini-jets”) in which the particle exhaust is confined to a very narrow opening angle must be invoked. Lyubarsky (2012) proposed a model involving quasi-cyclic instabilities near the base of the polar jet, which seems to be supported by full-scale simulations of the Crab Nebula (Porth et al. 2013). However, if the flares occur by discharge of accumulated magnetic energy, their power could sometimes exceed that of the pulsar, which has not been seen yet (meanwhile, our model would be ruled out by such observations). Arguments (e.g. Clausen-Brown & Lyutikov 2012) in favor of “accumulation-discharge” models appeal to the extreme stability of the pulsar as the nebula’s power supply. Be that as it may, wind plasma is an unsteady transmission line for delivery of

the pulsar's AC power to the nebula.

The author gratefully acknowledges Jon Arons for inspiring discussions, and thoughtful contributions from Mikhail Belyaev, Krzysztof Nalewajko, Yajie Yuan, Roger Blandford, Lorenzo Sironi, Jonathan Granot, An-

drew MacFadyen, and Tom Abel. Simulations were run on the Comet cluster at the San Diego Supercomputer Center (SDSC) through XSEDE grant AST150038, as well as Pleiades of the NASA High-End Computing (HEC) Program through the NASA Advanced Supercomputing (NAS) Division at Ames Research Center.

#### REFERENCES

- Abdo, A. A., Ackermann, M., Ajello, M., et al. 2011, *Science* (New York, N.Y.), 331, 739
- Aharonian, F. A., Bogovalov, S. V., & Khangulyan, D. 2012, *Nature*, 482, 507
- Balbo, M., Walter, R., Ferrigno, C., & Bordas, P. 2011, *Astronomy & Astrophysics*, 527, L4
- Bednarek, W., & Idec, W. 2011, *Monthly Notices of the Royal Astronomical Society*, 414, 2229
- Bhattacharjee, A., Huang, Y.-M., Yang, H., & Rogers, B. 2009, *Physics of Plasmas*, 16, 112102
- Bietenholz, M. F., Yuan, Y., Buehler, R., Lobanov, A. P., & Blandford, R. 2014, *Monthly Notices of the Royal Astronomical Society*, 446, 205
- Biskamp, D. 1986, *Physics of Fluids*, 29, 1520
- Blandford, R., East, W., Nalewajko, K., Yuan, Y., & Zrake, J. 2015a, arXiv:1511.07515
- Blandford, R., Yuan, Y., & Zrake, J. 2015b, *American Astronomical Society*
- Bogovalov, S. V. 1999, *Astronomy and Astrophysics*
- Brandenburg, A., Kahniashvili, T., & Tevzadze, A. G. 2015, *Physical Review Letters*, 114, 075001
- Bucciantini, N., Arons, J., & Amato, E. 2011, *Monthly Notices of the Royal Astronomical Society*, 410, 381
- Buehler, R., Scargle, J. D., Blandford, R. D., et al. 2012, *The Astrophysical Journal*, 749, 26
- Bykov, A. M., Pavlov, G. G., Artemyev, A. V., & Uvarov, Y. A. 2012, *Monthly Notices of the Royal Astronomical Society: Letters*, 421, L67
- Camus, N. F., Komissarov, S. S., Bucciantini, N., & Hughes, P. A. 2009, *Monthly Notices of the Royal Astronomical Society*, 400, 1241
- Cerutti, B., Philippov, A., Parfrey, K., & Spitkovsky, A. 2015, *Monthly Notices of the Royal Astronomical Society*, 448, 606
- Cerutti, B., Werner, G. R., Uzdensky, D. A., & Begelman, M. C. 2014a, *Physics of Plasmas*, 21, 056501
- . 2014b, *The Astrophysical Journal*, 782, 104
- Childress, S. 1970, *Journal of Mathematical Physics*, 11, 3063
- Clausen-Brown, E., & Lyutikov, M. 2012, *Monthly Notices of the Royal Astronomical Society*, 426, 1374
- Coroniti, F. V. 1990, *The Astrophysical Journal*, 349, 538
- Dombre, T., Frisch, U., Greene, J. M., et al. 1986, *Journal of Fluid Mechanics*, 167, 353
- East, W. E., Zrake, J., Yuan, Y., & Blandford, R. D. 2015, *Physical Review Letters*, 115, 095002
- Emmering, R. T., & Chevalier, R. A. 1987, *The Astrophysical Journal*, 321, 334
- Guo, F., Liu, Y.-H., Daughton, W., & Li, H. 2015, *The Astrophysical Journal*, 806, 167
- Harris, E. G. 1962, *Il Nuovo Cimento*, 23, 115
- Hoshino, M. 2012, *Physical review letters*, 108, 135003
- Huang, Y.-M., & Bhattacharjee, A. 2010, *Physics of Plasmas*, 17, 062104
- Inoue, T. 2012, *The Astrophysical Journal*, 760, 43
- Kelner, S. R., Aharonian, F. A., & Khangulyan, D. 2013, *The Astrophysical Journal*, 774, 61
- Kennel, C. F., & Coroniti, F. V. 1984, *The Astrophysical Journal*, 283, 710
- Kirk, J. G., & Skjaraasen, O. 2003, *The Astrophysical Journal*, 591, 366
- Komissarov, S. S. 2012, *Monthly Notices of the Royal Astronomical Society*, 428, 2459
- Kouzu, T., S. Tashiro, M., Terada, Y., et al. 2013, *Publications of the Astronomical Society of Japan*, 65, 74
- Lyubarsky, Y., & Kirk, J. G. 2001, *The Astrophysical Journal*, 547, 437
- Lyubarsky, Y. E. 2012, *Monthly Notices of the Royal Astronomical Society*, 427, 1497
- Madsen, K. K., Reynolds, S., Harrison, F., et al. 2015, *The Astrophysical Journal*, 801, 66
- McKinney, J. C. 2006, *Monthly Notices of the Royal Astronomical Society*, 367, 1797
- Meyer, M., Horns, D., & Zechlin, H.-S. 2010, *Astronomy & Astrophysics*, 523, A2
- Michel, F. C. 1973, *The Astrophysical Journal*, 180, 207
- . 1994, *The Astrophysical Journal*, 431, 397
- Olesen, P. 2015, arXiv:1509.08962
- Parker, E. N. 1958, *The Astrophysical Journal*, 128, 664
- Porth, O., Komissarov, S. S., & Keppens, R. 2013, *Monthly Notices of the Royal Astronomical Society*, 438, 278
- Radice, D., & Rezzolla, L. 2013, *The Astrophysical Journal*, 766, L10
- Rees, M. J., & Gunn, J. E. 1974, *Monthly Notices of the Royal Astronomical Society*, 167, 1
- Rudy, A., Horns, D., DeLuca, A., et al. 2015, *The Astrophysical Journal*, 811, 24
- Rybicki, G. B., & Lightman, A. P. 1979, *New York*
- Sironi, L., & Spitkovsky, A. 2011, *The Astrophysical Journal*, 741, 39
- . 2014, *The Astrophysical Journal*, 783, L21
- Striani, E., Tavani, M., Vittorini, V., et al. 2013, *The Astrophysical Journal*, 765, 52
- Sturrock, P., & Aschwanden, M. J. 2012, *The Astrophysical Journal*, 751, L32
- Tanaka, S. J., & Takahara, F. 2010, *The Astrophysical Journal*, 715, 1248
- Tavani, M., Bulgarelli, A., Vittorini, V., et al. 2011, *Science* (New York, N.Y.), 331, 736
- Taylor, J. B. 1974, *Physical Review Letters*, 33, 1139
- Teraki, Y., & Takahara, F. 2013, *The Astrophysical Journal*, 763, 131
- Uzdensky, D. A., Cerutti, B., & Begelman, M. C. 2011, *The Astrophysical Journal*, 737, L40
- Uzdensky, D. A., Loureiro, N. F., & Schekochihin, A. A. 2010, *Physical review letters*, 105, 235002
- Uzdensky, D. A., & Spitkovsky, A. 2014, *The Astrophysical Journal*, 780, 3
- Zelenyi, L. M., & Krasnosel'skikh, V. V. 1979, *Soviet Astronomy*, 23
- Zrake, J. 2014, *The Astrophysical Journal*, 794, L26
- Zrake, J., & East, W. E. 2015, arXiv:1509.00461
- Zrake, J., & MacFadyen, A. 2012, *The Astrophysical Journal Letters*
- Zrake, J., & MacFadyen, A. I. 2011, *The Astrophysical Journal*, 744, 32